

Using Internal Coordinates to Describe Photoinduced Geometry Changes in MLCT Excited States

Mark R. Waterland,^{*,†} Sarah L. Howell,^{‡,§} and Keith C. Gordon^{*,‡}

Institute of Fundamental Sciences, Massey University, Private Bag 11 222, Palmerston North, New Zealand, and MacDiarmid Institute for Advanced Materials and Nanotechnology, Department of Chemistry, University of Otago, PO Box 56, Dunedin, New Zealand

Received: January 17, 2007; In Final Form: March 8, 2007

A resonance Raman intensity analysis of the metal-to-ligand charge-transfer (MLCT) transition for the rhenium compound $\text{Re}(2-(2'\text{-pyridyl})\text{quinoxaline})(\text{CO})_3\text{Cl}$ (RePQX) is presented. Photoinduced geometry changes are calculated, and the results are presented using the vibrational normal modes and the redundant internal coordinates. A density functional theory calculation is used to determine the ground-state nonresonant Raman spectrum and a transformation matrix that transforms the redundant internal coordinates into the normal modes. The normal modes ν_{37} (rhenium coordination sphere distortion) and ν_{75} (ligand skeletal stretch) show the largest photoinduced geometry change ($\Delta = 1.0$ and 0.7 , respectively). A single carbonyl mode is enhanced in the resonance Raman spectra. Time-dependent density functional theory is used to calculate excited-state geometry changes, which are subsequently used to determine the signs of the photoinduced normal mode displacements. Transforming to internal coordinates reveals that all the CO bond lengths are displaced in the excited state. The Re–C and C–C ligand bond lengths are also displaced in the excited state. The results are discussed in terms of a simple one-electron picture for the electronic transition. Many bond angles and torsional coordinates are also displaced by the metal-to-ligand charge transfer, and most of these are associated with the rhenium coordination sphere. It is demonstrated that using internal coordinates presents a clear picture of the geometry changes associated with photoinduced electron transfer in metal polypyridyl systems.

1. Introduction

The interest in metal-to-ligand charge-transfer (MLCT) excited states of transition-metal compounds has intensified recently as a result of their application in a variety of photoelectrochemical devices such as dye-sensitized solar cells^{1–7} and organic light-emitting devices.^{8–12} In both of these applications, the electron-transfer properties of the photochemically or electrochemically generated MLCT state determine to a large extent the efficiency of these devices. The Marcus–Hush model^{13,14} states that the degree of structural distortion coupled to the charge-transfer process will determine the rate of electron transfer. Structural distortions also determine the rates of nonradiative decay from MLCT excited states via the so-called energy gap law.^{15–17} Therefore, excited-state structural distortions determine both the photo- and electrochemical properties of photoelectrochemical materials.

There are relatively few techniques capable of determining excited-state structural distortions, largely as a result of the transient nature of the excited state itself. Ground-state absorption and resonance Raman spectroscopy provide an approach to determining excited-state structural distortions.^{18,19} In both cases, the excited-state structural information is carried in the spectroscopic intensities. In absorption spectroscopy, the geometry changes along each vibrational mode are highly coupled

giving rise to hopelessly convoluted Franck–Condon progressions and broad MLCT transitions displayed by many transition-metal species. In resonance Raman spectroscopy, the resonance Raman excitation profiles (RREP) for each Franck–Condon active vibrational mode allow mode-specific geometry changes to be determined. A small number of resonance Raman intensity analyses for MLCT transitions have appeared,^{20–22} but these studies present the results using the normal coordinates that describe the vibrational modes. If the normal coordinates are highly delocalized, a more intuitive picture of the geometry changes can be obtained by transforming the normal coordinate geometry changes to changes along an appropriate set of internal coordinates, or Cartesian coordinates.²³ In this work, we show that such a transformation can be achieved using a normal coordinate analysis provided by density functional theory (DFT) calculations. The geometry changes are simply related to mode-specific reorganization energies,²⁴ thus, a resonance Raman intensity analysis (RRIA) allows a detailed analysis of the inner-sphere reorganization energy. An RRIA of the absolute resonance Raman intensities has the added advantage of providing an estimate of outer-sphere (solvent) reorganization energy.

Rhenium compounds show excellent photochemical stability and useful photophysical properties^{25–27} and are promising candidates as luminophores for organic light-emitting devices.^{28–30} As such, the electron-transfer properties of these materials are of interest. In particular for electron transfer between identical species (e.g., a hopping mechanism), electron-transfer rates will be maximized when the reorganization energies are minimized. In this paper, we perform an RRIA and determine the inner-

* To whom correspondence should be addressed. E-mail: M.Waterland@massey.ac.nz (M. W.); kgordon@alkali.otago.ac.nz (K. G.).

† Massey University.

‡ University of Otago.

§ Current address: Chemistry Department, School of Physical and Geographical Sciences, Lennard-Jones Laboratories, Keele University, Staffordshire, ST5 5BG, United Kingdom.

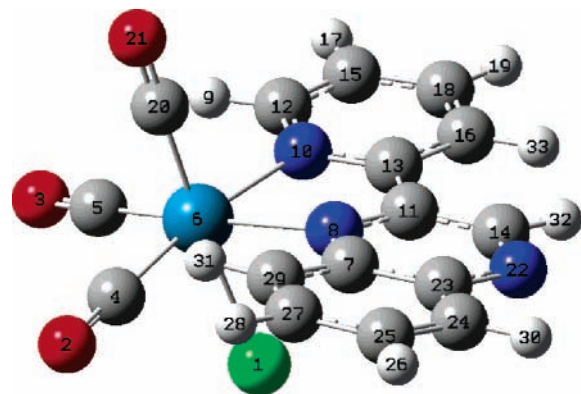


Figure 1. Structure and atom labels for $\text{Re}(\text{pqx})(\text{CO})_3\text{Cl}$ (RePQX).

and outer-sphere reorganization energies of the rhenium complex, *fac*- $\text{Re}(\text{pqx})(\text{CO})_3\text{Cl}$ (RePQX), where pqx is 2-(2'-pyridyl)-quinoxaline (Figure 1). We show that the geometry changes in the rhenium coordination sphere and π -acceptor ligands can be expressed in terms of changes along the bond lengths, bond angles, and torsional coordinates. The tricarbonylchlororhenium moiety is chosen as it provides a single MLCT transition to the polypyridyl acceptor ligand and π -acceptor carbonyl ligands that are excellent spectroscopic reporters on the geometry and oxidation state of the metal center.³¹ The small number of atoms in the rhenium coordination sphere simplifies the Raman spectrum and allows a facile comparison with vibrational frequencies calculated using density functional theory methods.

II. Experimental Section and Theory

$\text{Re}(\text{pqx})(\text{CO})_3\text{Cl}$ was prepared from $\text{Re}(\text{CO})_5\text{Cl}$ and 2-(2'-pyridyl)quinoxaline on the basis of literature methods.²¹ $\text{Re}(\text{CO})_5\text{Cl}$ was synthesized on the basis of literature procedures.³² The pqx ligand was synthesized according to literature procedures.²¹

Spectroscopic grade solvents were used for all spectroscopic measurements. Fourier transform infrared (FT-IR) spectra were collected, using a Perkin-Elmer Spectrum BX FT-IR system with Spectrum v.2.00 software, of potassium bromide (KBr) disks. Spectra were measured using 64 scans. Band positions are reproducible within 1–2 cm^{-1} . FT-Raman spectra were collected on powder samples, using a Bruker Equinox-55 FT-interferometer bench equipped with an FRA/106 Raman accessory and utilizing OPUS (version 5.0) software. An Nd:YAG laser with 1064 nm excitation wavelength was used. An InGaAs diode (D424) operating at room temperature was used to detect Raman photons. Spectra were typically measured using 16 scans at a power of 100 mW and a resolution of 4 cm^{-1} .

A continuous-wave Innova I-302 krypton-ion laser (Coherent, Inc.) or Melles Griot Omnichrome MAP-543 argon-ion laser was used to generate resonance Raman scattering. Band-pass filters removed the Kr^+ plasma emission lines from the laser output. The laser output was adjusted to give between 15 and 20 mW at the sample. The incident beam and the collection lens were arranged in a 135° back-scattering geometry to reduce Raman intensity reduction by self-absorption.³³ An aperture-matched lens was used to focus scattered light through a narrow band line-rejection (notch) filter (Kaiser Optical Systems) and a quartz wedge (Spex) and onto the 100 μm entrance slit of a spectrograph (Acton Research SpectraPro 500i). The collected light was dispersed in the horizontal plane by a 1200 grooves/mm ruled diffraction grating (blaze wavelength 500 nm) and was detected by a liquid-nitrogen-cooled back-illuminated Spec-

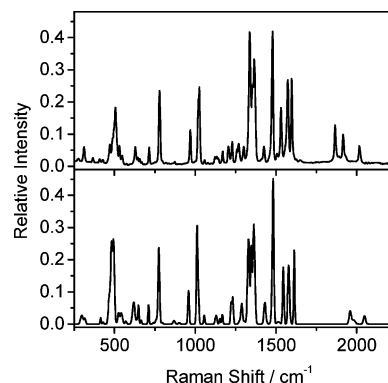


Figure 2. Experimental (top) and calculated (bottom) nonresonant Raman spectra for RePQX.

10:100B CCD controlled by a ST-133 controller and WinSpec/32 (version 2.5.8.1) software (Roper Scientific, Princeton Instruments).

Wavenumber calibration was performed using Raman bands from a 1:1 (by volume) mixture of acetonitrile and toluene sample.³⁴ (The ASTM subcommittee on Raman spectroscopy has adopted eight materials as Raman shift standards (ASTM E 1840). The band wavenumbers for these standards are available at <http://chemistry.ohio-state.edu/~rmccreer/shift.html>.) Peak positions were reproducible to within 1–2 cm^{-1} . Spectra were obtained with a resolution of 5 cm^{-1} . Freshly prepared samples were held in a spinning NMR tube. The concentration of the solute was 5 mmol dm^{-3} . Spectral intensities were corrected for self-absorption,³⁵ differential band pass, and throughput of the spectrograph and detector sensitivity. Integrated band intensities were obtained using the peak-fitting module in Origin Pro 7.5. Solute Raman cross sections were obtained relative to the 702/740 cm^{-1} doublet of dichloromethane.³⁶ Resonance Raman spectra were obtained with excitation wavelengths of 413.1, 457.9, 488.0, 514.5, and 530.1 nm.

Electronic absorption spectra were recorded on a Varian Cary 500 scan UV–vis–NIR spectrophotometer, with Cary WinUV software. Samples were typically $\sim 10^{-4}$ mol dm^{-3} .

Simulations. The absorption and resonance Raman intensities were simulated using the time-dependent formulation originally developed by Lee and Heller^{37–39} and subsequently implemented and summarized by Myers.^{18,40} The Raman amplitude between the initial and final vibrational states, α_{if} , is calculated as the half-Fourier transform of the time-dependent overlap of a wavepacket propagating on the resonant electronic excited and the $v'' = 1$ ground electronic state vibrational wavefunction:

$$\alpha_{if}(\omega_L, \delta) = \frac{1}{\hbar} \int_0^\infty dt \langle \chi_f | \chi_i(t) \rangle \exp[i(\omega_L - \omega - \delta + \omega_i)t - g(t)]$$

where ω_L is the incident laser frequency, $\hbar\omega_i$ is the energy of the initial vibrational level (set to zero as scattering from all modes in the simulation occurs from the ground vibrational level), ω is the zero–zero electronic transition frequency, and δ is the electronic zero–zero frequency shift due to inhomogeneous broadening. $\langle \chi_f |$ and $\langle \chi_i |$ are the multidimensional ground-state vibrational wavefunctions multiplied by the transition dipole moment and $|\chi_i(t)\rangle = \exp(-iHt/\hbar)|\chi_i\rangle$ is the initial vibrational wavefunction propagated for a time, t , on the electronic excited-state surface, by the excited-state vibrational Hamiltonian. $g(t)$ is the solvent-broadening

function, modeled as an overdamped Brownian oscillator.⁴¹ Separable harmonic oscillators, with frequencies taken from the ground-state Raman modes, were used in the model for the potential energy surfaces. The ground- and excited-state normal modes are assumed to have the same form, that is, Dushinsky rotation is not included, and non-Condon effects were not included.

The experimental observable, the differential Raman cross section, is calculated via

$$\left(\frac{d\sigma}{d\Omega}\right)_{\parallel+\perp} = \sum_i B_i \sum_f \int d\omega_s \left(\frac{\omega_s^3 \omega_L}{c^4} \int_{-\infty}^{+\infty} d\delta G(\delta) \left| \alpha_{if}(\omega_L, \delta) \right|^2 \right) L_{if}(\omega_L - \omega_s)$$

where B_i is the Boltzmann population of the initial vibrational state (assumed to be unity here) and $L_{if}(\omega_L - \omega_s)$ is a Raman line-shape function. $G(\delta)$ is a normalized inhomogeneous broadening function which is taken to be Gaussian.

The absorption cross section is calculated at the same level of theory using

$$\sigma_A(\omega_L) = \frac{4\pi|\mu|^2\omega_L}{3n\hbar c} \sum_i B_i \int_{-\infty}^{+\infty} d\delta G(\delta) \text{Re} \int_{-\infty}^{+\infty} dt \langle \chi_i | \chi_i(t) \rangle \exp[i(\omega_L - \omega - \delta + \omega_i)t - g(t)]$$

where the real part of the Fourier transform is taken and n is the refractive index of the solvent.

Calculations. The geometry, the vibrational frequencies, and their IR and Raman intensities were calculated using DFT calculations (B3LYP functional) with a 6-31G(d) basis set on all atoms except Re for which a LANAL2DZ ECP was used. These were implemented with the Gaussian 03W program package.⁴² The visualization of the vibrational modes was provided by the Molden package⁴³ and GaussViewW (Gaussian Inc.). Frequency calculations on the complexes produced no imaginary frequencies indicating that in each case the minimum energy point was located. The Raman intensities are calculated from the Raman activity for 1064 nm excitation.^{44–46}

The frequencies were scaled by 0.975 as this was found to give the lowest mean absolute deviation between experimental and calculated data.

III. Results and Discussion

III.a. Nonresonant Raman Spectra. The calculated and experimental nonresonant Raman spectra are shown in Figure 2. The DFT calculations provide a complete description of the normal modes in the nonresonant Raman and IR spectra, and a subset of these modes are enhanced in the resonance Raman spectra. It is important, therefore, to assess the quality of the DFT calculations. The calculated ground-state Raman and IR intensities provide a useful benchmark for the reliability of the calculations established, the dimensionless displacements along each normal mode enhanced in the resonance Raman spectrum are then related to the geometry changes using the descriptions of the normal modes. For the modes with frequencies less than 1650 cm^{-1} , the mean absolute deviation between experimental and calculated frequencies (after scaling by 0.975) is 6.8 cm^{-1} (43 modes observed), demonstrating excellent agreement between calculated and observed frequencies. Figure

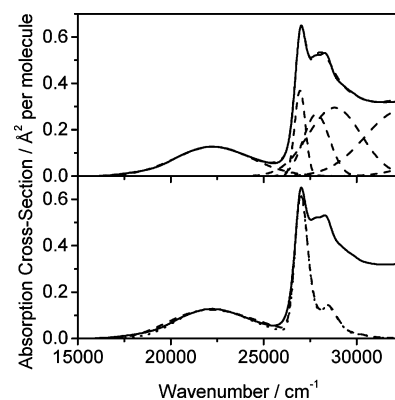


Figure 3. Electronic absorption spectra for RePQX. The top trace shows a sum-of-Gaussians fit to the experimental data. Lower trace shows the line shape simulated using time-dependent wavepacket methods with two electronic states.

2 shows the very satisfactory agreement between the calculated and experimental intensities. The majority of these modes are largely associated with the pqx ligand and the five-member Re α -diimine ring. The calculated frequencies of the modes involving the carbonyl ligands, 1959 (ν_{82}), 1980 (ν_{83}), and 2048 (ν_{84}) cm^{-1} , show slightly poorer agreement with experiment 1867.2, 1919.2, and 2017.6 cm^{-1} . However, the relative intensities are well reproduced in the calculated spectra. The strongest features in the nonresonant Raman spectrum (obtained with 1064 nm excitation) below 1650 cm^{-1} appear at 781 (771, ν_{44}), 972 (959, ν_{53}), 1028 (1022, ν_{57}), 1338.7 (1330, ν_{69}), 1367.6 (1363, ν_{71}), 1481.4 (1482, ν_{75}), 1533.5 (1545, ν_{77}), 1575.9 (1578, ν_{78}), and 1599.1 (1613, ν_{80}) cm^{-1} . The calculated frequencies and mode numbers are given in parentheses.

III.b. Electronic Spectrum. The electronic absorption spectrum of RePQX in dichloromethane solution is shown in Figure 3. A broad, low-intensity band, peaked at 22 200 cm^{-1} , is assigned to a metal-to-ligand charge-transfer band, on the basis of the absence of this band from both the free ligand and $\text{Re}(\text{CO})_5\text{Cl}$ precursor species. Other polypyridyl systems containing the pqx ligand^{21,47} exhibit similar low-intensity bands at low energy. On the basis of TDDFT calculations, we assign this band to a one-electron transition from MO85 to MO87. Also shown in Figure 3 is a sum-of-Gaussians fit to the absorption spectrum. The MLCT band is very closely fit by a single Gaussian function, indicating that the charge-transfer transition contains just a single electronic origin.

The electronic spectrum exhibits sharper features at higher energy (around 28 000 cm^{-1}) that are very similar to the free-ligand absorption bands and therefore correspond to ligand-centered (LC) bands in the metal complex. The band shape is complex and the sum-of-Gaussians fit uses a minimal number of Gaussians to approximate the experimental spectrum. The Gaussian fit is used to guide the simulation of the electronic spectrum using the time-dependent theory. As indicated below, the time-dependent theory suggests that at least part of the structure of the LC band is due to vibronic structure rather than to multiple electronic origins. One may expect that the intensity and proximity of the LC bands to the MLCT band would lead to interference^{23,48,49} in the resonance Raman excitation profiles. The LC transitions have a complicated band structure and although two electronic states are included in the time-dependent simulations of the absorption spectrum and resonance Raman profiles, it is clear from the sum-of-Gaussian fit that more electronic states could be included in the simulations. However, without resonance, Raman data taken with excitation on resonance across the LC band adding additional electronic states

TABLE 1: Normal-Mode Displacements and Reorganization Energies for the MLCT State of RePQX^a

mode	expt freq (cm ⁻¹)	calcd freq (cm ⁻¹)	\Delta	\lambda (cm ⁻¹)
21	425	415	0.4	29
25	490	481	0.9	185
28	503	496	0.9	186
30	533	526	0.2	12
34	572	570	0.3	26
37	630	623	1.0	315
51	971	952	0.3	50
55	982	982	0.3	36
56	1022	1012	0.2	13
57	1028	1022	0.4	63
69	1339	1330	0.3	60
71	1368	1363	0.3	62
75	1481	1482	0.7	363
77	1534	1545	0.3	69
78	1576	1578	0.2	38
80	1599	1613	0.2	32
84	2018	2048	0.5	204

^a Electronic parameters: electronic origin 16900 cm⁻¹, Brownian oscillator parameters $D = 2900$ cm⁻¹, $\Lambda = 290$ cm⁻¹, transition dipole length 0.650 Å, $T = 298$ K, and zero inhomogeneous broadening.

would add a large number of unrestrained additional parameters (to describe the electronic properties of the additional states and the dimensionless displacements for each coupled vibration).

The simulated absorption spectrum is shown in the lower panel of Figure 3. The foot of Table 1 summarizes the parameters used to fit the absorption and resonance Raman spectra. During the fitting procedure, two limiting cases for the electronic parameters were obtained. In one case, an excellent fit to the red edge of the MLCT band is obtained, but the total width of the absorption band is overestimated, because of a large amount of homogeneous broadening. In the other case, a smaller value for the homogeneous broadening is used, and as a result, the absorption band is narrower. The simulated spectrum fits more closely the peak of the experimental curve, however, the fit to the red edge is less satisfactory. The Raman intensities are used to guide the fitting procedure and only by using the smaller value for the homogeneous broadening can the Raman intensities be accurately simulated. A value of 2900 cm⁻¹ is used for the homogeneous broadening in this case which corresponds to a solvent reorganization energy of 3790 cm⁻¹ which is a physically reasonable value for this parameter in a polar organic solvent.^{36,50}

III.c. Resonance Raman Spectra. Resonance Raman spectra obtained with 413 and 514 nm excitation are shown in Figure 4. The spectra are superficially similar with most modes above 700 cm⁻¹ indicating similar enhancements at both wavelengths. Below 700 cm⁻¹, the intensities of the modes at 490 (ν_{25}), 501 (ν_{28}), and 630 cm⁻¹ (ν_{37}) show stronger enhancement with 514 nm excitation. The mode assignments from the DFT calculations indicate that these modes have significant amplitude involving atoms in the pqx ligand. These modes would also couple to the LC transition and therefore are most likely to show interference effects between Raman scattering amplitudes from the LC and MLCT states. This could either result in constructive or destructive interference, and it would appear from the Raman intensities obtained with 413 nm excitation that destructive interference results in a decrease in the intensities of these modes relative to longer wavelength excitation. The resonance Raman spectra obtained with longer wavelength excitation exhibit an intensity pattern with “pure” MLCT character. Plots of two of the modes are shown in Figure 5. Mode 37 (628 cm⁻¹) contains a metal carbonyl bend component and an appreciable contribu-

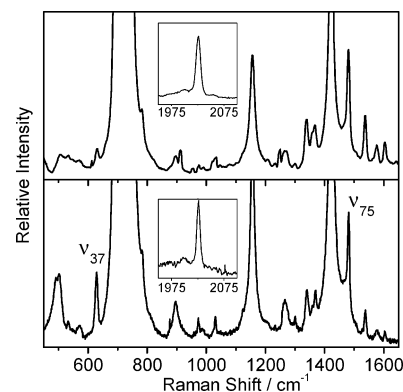


Figure 4. Resonance Raman spectra for RePQX taken with 413 nm (top) and 514.5 nm (bottom) excitation. Solvent bands (dichloromethane) appear at 701/740, 1156, and 1423 cm⁻¹. The insets show the carbonyl mode enhancements.

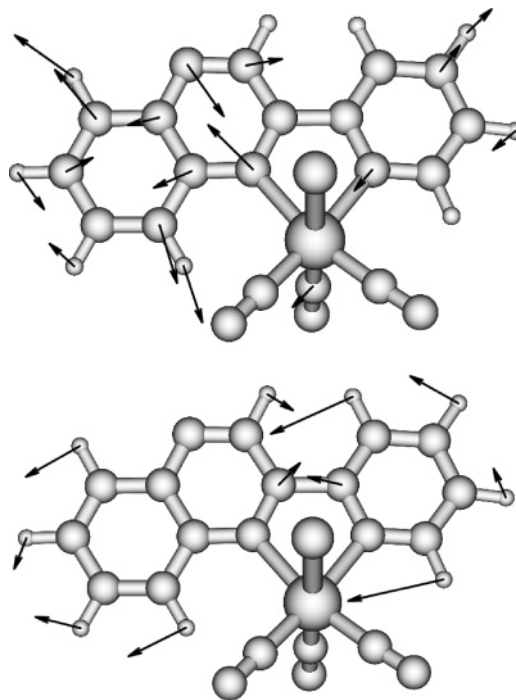


Figure 5. Plots of vibrational modes 37 (top) and 75 (bottom) for RePQX.

tion from an in-plane bend of the pqx ligand. Mode 75 is largely localized to the pqx ligand.

The Raman excitation profiles for ν_{37} , ν_{71} , ν_{75} , and ν_{78} are shown in Figure 6. The simulated profiles closely follow the experimental data for excitation on the red edge of the MLCT band but deviate as the excitation energy approaches the red edge of the LC band. This is most likely because of interference effects from the higher energy and more intense LC transitions. The bottom panel of Figure 3 shows that our simulations reproduce the lowest energy LC electronic transition and also indicates that some of the structure of the LC transition is due to vibronic progressions, as suggested above. Our simulations include two electronic states (MLCT and LC) that contribute to the Raman scattering amplitude, but the upper panel of Figure 3 suggests at least one more additional state is required to reproduce the absorption spectrum. Because we could not obtain resonance Raman data for excitation into the LC band, including additional states in the simulations would introduce several unconstrained parameters into the model and would lead to uncertainty in the values of the optimized parameters. Because

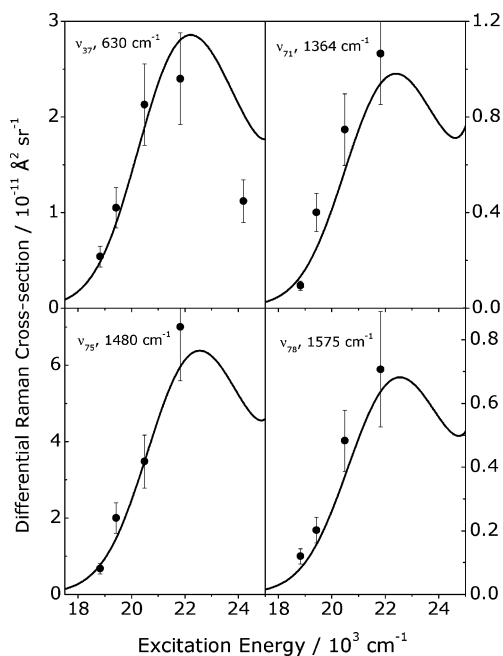


Figure 6. Raman excitation profiles for the MLCT transition of RePQX in dichloromethane. Excitation wavelengths were 413.1, 457.9, 488.0, 514.5, and 530.1 nm.

of the interference effects observed with higher energy excitation, more emphasis was placed on accurately fitting the Raman intensities obtained on resonance with the red edge of the MLCT transition. Because the same parameters are used to fit the Raman intensities for at least three different excitation energies, the simulations provide accurate estimates of the electronic and nuclear parameters that describe the MLCT transition.

Mode 37 undergoes the largest displacement ($\Delta = 1.0$) following the MLCT transition. Figure 5 shows that this mode largely involves deformation of the pqx ligand but also contains significant contributions from the rhenium coordination sphere. Figure 7 displays the molecular orbitals (MO85 and MO87) that contribute to the lowest energy transition with the largest oscillator strength. These orbitals are similar in nature to those calculated with DFT for a related system, *fac*-[Re(bpy)(CO)₃-(4-Etpy)]⁺, using a B3LYP/LANL2 model,³¹ with a significant amount of electron density on the CO ligands. In a simple one-electron picture, the MO plots describe the lowest energy transition as a transfer of electron density from MO85 to MO87 which results in an increase in the electron density in the π^* -orbital of pqx (MO87), that is, formation of the pqx radical anion. The MO plot also shows a large change in the bonding character of the carbonyl ligands with MO87 possessing more CO bonding character than MO85. Considering the MO plots, the MLCT transition is perhaps more accurately described as a redistribution of the ligand π -electron system. The electron density in the Re–N bonds is only slightly unperturbed by the electronic transition. The simple one-electron transition and MO plots are consistent with the enhancements seen in the resonance Raman spectra. The enhanced modes all contain motion of the pqx ligand to a greater or lesser degree and the electronic structure calculations show that it is the ligands' electron density that is mostly perturbed by the electron transition. The large displacement along other low-frequency modes that involve angular deformations and torsional motion about the rhenium center (ν_{25} and ν_{28}) is consistent with this interpretation as is the relatively large displacement along ν_{84} . Other modes that

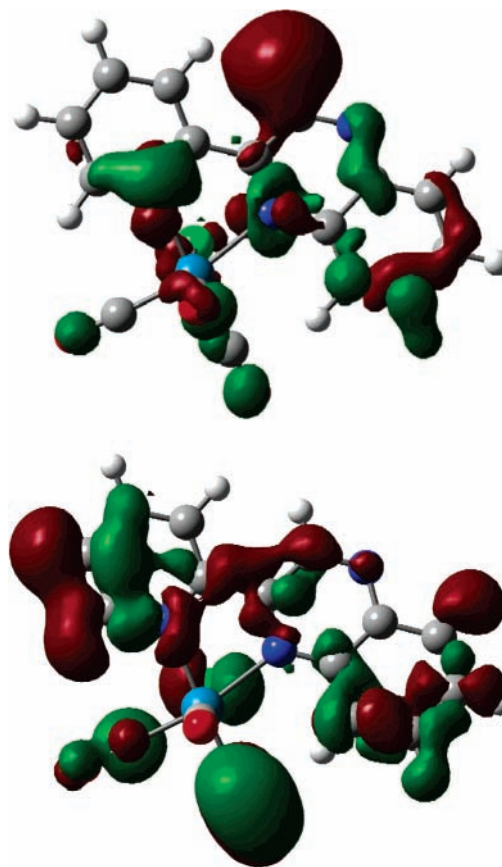


Figure 7. Molecular orbitals that contribute to the MLCT transition. MO85 (top) and MO87 (bottom).

show significant displacement are the vibrational modes of the pqx ligand (between 1300 and 1650 cm^{-1}). Of these, ν_{75} has the largest dimensionless displacement of $\Delta = 0.7$.

III.d. Mode Displacements along Internal Coordinates.

However useful these qualitative interpretations are, the highly delocalized nature of both the molecular orbitals and the vibrational modes prevents a more intuitive interpretation in terms of changes along the bond lengths and bond angles of the molecule. In favorable cases, for small molecules the displacements along normal modes can be interpreted in terms of changes along bond lengths and angles.⁵¹ However, this is quite often difficult for large molecules with delocalized modes.

A transformation from the dimensionless displacements along the normal modes to the displacements along the internal coordinates of the molecule can help with the interpretation of the resonance Raman intensity analysis. The transformation follows a similar procedure to that described by Lilichenko et al.²³ The normal-mode analysis of the ground state of RePQX from the Gaussian03 output provides all the necessary information to transform from the normal coordinates to the redundant internal coordinates. The resonance Raman intensities are determined by wavepacket motion on the excited-state surface along the excited-state normal modes; for our transformation, we implicitly assume that the ground-state and excited-state normal modes are similar. This approximation is used consistently in the empirical modeling of the resonance Raman intensities where no Duchinsky rotation of the excited state relative to the ground state is assumed. A computational procedure such as Vibrational Projection Analysis^{52,53} may be used to determine the extent of mode mixing in the excited state,

although this requires an expensive calculation of the excited-state frequencies.

The output from the normal-mode analysis is used to form a matrix, \mathbf{S} , that transforms from redundant internal coordinates, \mathbf{R} , to normal coordinates, \mathbf{Q} , that is,

$$\mathbf{Q} = \mathbf{S}\mathbf{R} \quad (1)$$

The matrix that performs the inverse transformation, that is, from normal coordinates to redundant internal coordinates, is required. Because the redundant internal coordinates are linearly dependent, \mathbf{S} is a nonsquare matrix, and thus the pseudoinverse of \mathbf{S} must be found. The Moore–Penrose algorithm, as implemented in the Mathematica suite, is used to determine the pseudoinverse of \mathbf{S} (the Moore–Penrose inverse satisfies $\mathbf{S}\mathbf{S}^\dagger\mathbf{S} = \mathbf{S}$ and $\mathbf{S}^\dagger\mathbf{S}\mathbf{S}^\dagger = \mathbf{S}^\dagger$). The inverse transformation is then

$$\mathbf{R} = \mathbf{S}^\dagger\mathbf{Q} \quad (2)$$

Thus, the dimensionless displacements along normal coordinates, Δ , are transformed to the dimensionless displacements along internal coordinates, δ :

$$\delta = \mathbf{S}^\dagger\Delta \quad (3)$$

The transformation requires the signed displacements. Because RePQX has 17 resonance Raman active vibrational modes, there are 2^{17} possible combinations of displacements that are consistent with the resonance Raman intensities. Computational studies can greatly assist in eliminating the majority of these combinations and can be used to compute excited-state gradients and displacements directly.^{23,54–56} In the case of the RePQX system, the lowest energy triplet-state geometry is an appropriate model for the resonant excited-state geometry probed in the resonance Raman experiments.²⁹ By calculating the triplet-state geometry, signed normal-mode displacements were determined in the following manner: first, changes along each internal coordinate were calculated between the ground (singlet) and excited (triplet) states. Then, by assuming the singlet- and triplet-state normal modes to be similar, the transformation matrix \mathbf{S} was used to transform the internal coordinate displacements to normal-mode displacements (eq 1). Table 1S contains geometry changes along selected internal coordinates (see Supporting Information). Alternatively, the geometry of the ligand radical anion may be used as a model for the excited-state geometry of the complex, and the neutral ligand may be used as a model for the ground-state.^{57,58} Although computationally less demanding, this approach requires qualitative arguments to determine the normal-mode displacements for the modes involving the rhenium atom and provides less satisfactory results.

Approximately three-quarters of the normal-mode displacements determined *ab initio* have values that are less than 15% of the maximum calculated displacement. This agrees well with the relatively small number of enhanced modes observed in the resonance Raman spectra. The *ab initio* displacements also give the correct intensity distribution for the three carbonyl modes and correctly predict modes 75 and 37 to have the largest displacements of the observed modes. The calculated normal-mode displacements for all enhanced modes can be found in the Supporting Information (Table 2S). These results provide confidence that the signs for the displacements of the enhanced modes in the resonance Raman spectra were determined correctly by the triplet-state geometry calculation. The magnitudes were taken from Table 1.

Using the signs determined by the *ab initio* calculations and the magnitudes taken from fitting the experimental data, the

TABLE 2: Displacements Following MLCT Excitation for Selected Redundant Internal Coordinates

$R(i,j)$	$\delta(R_{ij})$	$R(i,j,(k))$	$\delta(R_{ij(k)})$
$R(20,21)$	−0.20	$R(9,12)$	0.02
$R(3,5)$	−0.34	$R(16,33)$	0.02
$R(2,4)$	0.11	$R(14,32)$	0.02
$R(6,20)$	−0.57	$R(24,30)$	−0.01
$R(5,6)$	−0.91	$R(25,26)$	−0.03
$R(4,6)$	−0.18	$R(27,28)$	−0.03
$R(10,13)$	−0.60	$A(8,7,23)$	−0.55
$R(8,11)$	−0.40	$A(8,7,29)$	0.39
$R(11,13)$	0.40	$A(7,8,11)$	0.46
$R(6,8)$	0.20	$A(11,14,22)$	−0.35
$R(6,10)$	−0.20	$A(11,13,16)$	−0.41

transformation from normal modes to internal coordinates was carried out using eq 3. The results of the transformation for selected internal coordinates are displayed in Table 2. It should be stressed that dimensionless displacements result from the transformation procedure. As a check for self-consistency, the δ_i for the three CO and Re–C bonds (see Figure 1 for the numbering scheme) were used to determine the dimensionless displacements, Δ_j , for the carbonyl normal modes (i.e., ν_{82} , ν_{83} , ν_{84}):⁵⁹

$$\Delta_{82} = 0.34R_{2,4} + 0.55R_{3,5} - 0.20R_{4,6} - 0.32R_{5,6} - 0.73R_{6,20} - 1.24R_{20,21} = -8.1 \times 10^{-5}$$

$$\Delta_{83} = -1.00R_{2,4} + 0.96R_{3,5} + 0.58R_{4,6} - 0.57R_{5,6} - 0.09R_{6,20} + 0.16R_{20,21} = 5 \times 10^{-3}$$

$$\Delta_{84} = 0.92R_{2,4} + 0.84R_{3,5} - 0.55R_{4,6} - 0.50R_{5,6} - 0.37R_{6,20} + 0.62R_{20,21} = 0.42$$

As expected, only the “totally symmetric” carbonyl mode, ν_{84} , is calculated to have any appreciable displacement (and therefore intensity) on the basis of the resonance Raman intensity analysis and normal coordinate analysis.

Table 2 shows that despite only a single CO normal mode being resonantly enhanced, all three CO bond stretches are significantly displaced by the MLCT transition. A similar conclusion was reached by Gamelin et al.⁵⁹ and Dattelbaum and co-workers^{31,60} for similar rhenium carbonyl species. Gamelin et al. used time-resolved infrared spectroscopy and performed a normal coordinate analysis by using isotopic substitution whereas Dattelbaum and co-workers used DFT calculations to provide the normal coordinate analysis.⁵⁹ For RePQX, a pure Re–C normal mode is difficult to identify but transforming the displacements to internal coordinates shows that the Re–C bonds are all perturbed by the photoinduced electron transfer. The Re–N bonds, $R(6,8)$ and $R(6,10)$, show smaller displacements. It was noted above that the electron density between the Re and N atoms is largely unperturbed during the MLCT transition which is consistent with the small displacements along these coordinates. It is interesting to note the different magnitudes of the displacements for the Re–C and CO bond lengths. The low symmetry of the coordination sphere allows different displacements for the three Re–C and CO bond lengths. The displacements along the internal coordinates indicate the degree of asymmetry in the coordination sphere. The coordination sphere contains a π -donor ligand and several π -acceptor ligands, and the displacements demonstrate the varying electronic properties of these coordinating ligands. A recent study of *fac*-[Re(bpy)(CO)₃(4-Etpy)]⁺,³¹ using ultrafast time-resolved infra-

red spectroscopy and DFT calculations, determined the photo-induced geometry changes in the rhenium coordination sphere and found that all three CO bonds decrease in length following photoexcitation. Table 2 shows that two of the CO bond lengths in RePQX also show a decrease while the third (trans to the pyridyl ring of the pqx ligand) shows a slight bond length increase. Using the internal coordinate picture, the geometry changes are clear, and the largest changes occur in the rhenium coordination sphere and the quinoxaline portion of the poly-pyridyl ligand.

The bond length changes are consistent with a simple one-electron picture of the MLCT transition. For instance, the C–C bond stretches of the pqx ligand are all displaced as a result of the redistributed ligand π electron density. The ligand σ electron density is largely unperturbed, hence, the C–H bonds show only minor displacements. Table 2 also lists the displacements for selected angles; several angles of the rhenium coordination sphere are perturbed, along with the angles in the quinoxaline ring. The torsional modes with the largest displacements are localized to the rhenium coordination sphere. By inspecting the normal modes alone, the angular and torsional displacements are not obvious and a clear picture of the geometry changes around the rhenium center is only obtained when the displacements along the internal modes are considered.

The asymmetrical displacements in the coordination sphere have important implications in the rational design of electroluminescence that undergo facile electron-transfer processes. By controlling the displacements that accompany either oxidation or reduction of the electroluminescence, charge-transfer rates can be maximized by matching the total reorganization energy to the reaction free energy. By correlating ligand properties with coordinate-specific displacements, a rational method for the design of efficient electroluminescence could be developed. Minimizing geometry distortions in the MLCT state will also increase the rate of radiative decay back to the ground state, via the energy gap law,^{15–17,31} leading to further improvements in the efficiency of transition-metal-based OLED devices.

IV. Conclusions

This discussion demonstrates that the internal coordinates present a clear picture of the geometry changes following the MLCT transition, and these changes are consistent with simple MO theory descriptions of the charge-transfer process. By examining the normal modes alone, the geometry changes, particularly in the rhenium coordination sphere, are not obvious. Although both the normal-mode basis and the internal coordinate basis provide a complete description of the photoinduced geometry changes, the internal coordinates present these changes in a more intuitive fashion.

Acknowledgment. M. R. W. thanks the Royal Society of New Zealand for the award of a Fast-Start Marsden Grant (02-MAU-211). We thank the Foundation for Research Science and Technology and the MacDiarmid Institute for financial support of this work. We thank Timothy Simpson for preparing the pqx ligand.

Supporting Information Available: Tables of calculated changes along redundant internal coordinates for RePQX and calculated normal-mode displacements for resonance Raman enhanced normal modes are available. This material is available free of charge via the Internet at <http://pubs.acs.org>.

References and Notes

- Hagfeldt, A.; Gratzel, M. *Acc. Chem. Res.* **2000**, *33*, 269.
- Wang, P.; Humphry-Baker, R.; Moser, J. E.; Zakeeruddin, S. M.; Gratzel, M. *Chem. Mater.* **2004**, *16*, 3246.
- Gratzel, M. *Inorg. Chem.* **2005**, *44*, 6841.
- Nazeeruddin, M. K.; Angelis, F. D.; Fantacci, S.; Selloni, A.; Viscardi, G.; Liska, P.; Ito, S.; Takeru, B.; Gratzel, M. *J. Am. Chem. Soc.* **2005**, *127*, 16835.
- Wang, Q.; Zakeeruddin, S. M.; Nazeeruddin, M. K.; Humphry-Baker, R.; Gratzel, M. *J. Am. Chem. Soc.* **2006**, *128*, 4446.
- Wang, P.; Klein, C.; Moser, J. E.; Humphry-Baker, R.; Cevey-Ha, N. L.; Charvet, R.; Comte, P.; Zakeeruddin, S. M.; Gratzel, M. *J. Phys. Chem. B* **2004**, *108*, 17553.
- Nazeeruddin, M. K.; Klein, C.; Liska, P.; Gratzel, M. *Coord. Chem. Rev.* **2005**, *249*, 1460.
- Baldo, M. A.; O'Brien, D. F.; You, Y.; Shoustikov, A.; Sibley, S.; Thompson, M. E.; Forrest, S. R. *Nature* **1998**, *395*, 151.
- Baldo, M. A.; Thompson, M. E.; Forrest, S. R. *Nature* **2000**, *403*, 750.
- Brooks, J.; Babayan, Y.; Lamansky, S.; Djurovich, P. I.; Tsyba, I.; Bau, R.; Thompson, M. E. *Inorg. Chem.* **2002**, *41*, 3055.
- Lamansky, S.; Djurovich, P.; Murphy, D.; Abdel-Razzaq, F.; Lee, H. E.; Adachi, C.; Burrows, P. E.; Forrest, S. R.; Thompson, M. E. *J. Am. Chem. Soc.* **2001**, *123*, 4304.
- Lamansky, S.; Djurovich, P.; Murphy, D.; Abdel-Razzaq, F.; Kwong, R.; Tsyba, I.; Bortz, M.; Mui, B.; Bau, R.; Thompson, M. E. *Inorg. Chem.* **2001**, *40*, 1704.
- Barbara, P. F.; Meyer, T. J.; Ratner, M. A. *J. Phys. Chem.* **1996**, *100*, 13148.
- Marcus, R. A.; Sutin, N. *Biochim. Biophys. Acta* **1985**, *811*, 265.
- Caspar, J. V.; Kober, E. M.; Sullivan, B. P.; Meyer, T. J. *J. Am. Chem. Soc.* **1982**, *104*, 630.
- Caspar, J. V.; Meyer, T. J. *J. Phys. Chem.* **1983**, *87*, 952.
- Caspar, J. V.; Westmoreland, T. D.; Allen, G. H.; Bradley, P. G.; Meyer, T. J.; Woodruff, W. H. *J. Am. Chem. Soc.* **1984**, *106*, 3492.
- Myers, A. B. Excited Electronic State Properties from Ground-State Resonance Raman Intensities. In *Laser Techniques in Chemistry*; Myers, A. B., Rizzo, T. R., Eds.; John Wiley & Sons, Inc.: New York, 1995; Vol. 23, pp 325–384.
- Myers, A. B. *Acc. Chem. Res.* **1997**, *30*, 519.
- Thompson, D. G.; Schoonover, J. R.; Timpson, C. J.; Meyer, T. J. *J. Phys. Chem. A* **2003**, *107*, 10250.
- Waterland, M. R.; Howell, S. L.; Gordon, K. C.; Burrell, A. K. *J. Phys. Chem. A* **2005**, *109*, 8826.
- Howell, S. L.; Gordon, K. C.; Waterland, M. R.; Leung, K. H.; Phillips, D. L. *J. Phys. Chem. A* **2006**, *110*, 11194.
- Lilichenko, M.; Tittelbach-Helmrich, D.; Verhoeven, J. W.; Gould, I. R.; Myers, A. B. *J. Chem. Phys.* **1998**, *109*, 10958.
- Myers, A. B. *Chem. Rev.* **1996**, *96*, 911.
- Wolf, M. O.; Wrighton, M. S. *Chem. Mater.* **1994**, *6*, 1526.
- Christ, C. S.; Yu, J.; Zhao, X. H.; Palmore, G. T. R.; Wrighton, M. S. *Inorg. Chem.* **1992**, *31*, 4439.
- Fredericks, S. M.; Luong, J. C.; Wrighton, M. S. *J. Am. Chem. Soc.* **1979**, *101*, 7415.
- Lundin, N. J.; Walsh, P. J.; Howell, S. L.; McGarvey, J. J.; Blackman, A. G.; Gordon, K. C. *Inorg. Chem.* **2005**, *44*, 3551.
- Walsh, P. J.; Gordon, K. C.; Lundin, N. J.; Blackman, A. G. *J. Phys. Chem. A* **2005**, *109*, 5933.
- Lundin, N. J.; Blackman, A. G.; Gordon, K. C.; Officer, D. L. *Angew. Chem., Int. Ed.* **2006**, *45*, 2582.
- Dattelbaum, D. M.; Martin, R. L.; Schoonover, J. R.; Meyer, T. J. *J. Phys. Chem. A* **2004**, *108*, 3518.
- Schmidt, S. P.; Trogler, W. C.; Basolo, F. *Inorg. Synth.* **1990**, *28*, 160.
- Shriver, D. F.; Dunn, J. B. R. *Appl. Spectrosc.* **1974**, *28*, 319.
- McCreery, R. L. *Raman Spectroscopy for Chemical Analysis*; John Wiley & Sons, Inc.: New York, 2000.
- Myers, A. B.; Li, B. L.; Ci, X. P. *J. Chem. Phys.* **1988**, *89*, 1876.
- Egolf, D. S.; Waterland, M. R.; Kelley, A. M. *J. Phys. Chem. B* **2000**, *104*, 10727.
- Heller, E. J. *Acc. Chem. Res.* **1981**, *14*, 368.
- Lee, S. Y.; Heller, E. J. *J. Chem. Phys.* **1979**, *71*, 4777.
- Tannor, D. J.; Heller, E. J. *J. Chem. Phys.* **1982**, *77*, 202.
- Myers, A. B.; Mathies, R. A. Resonance Raman intensities: A probe of excited-state structure and dynamics. In *Biological Applications of Raman Spectroscopy*; Spiro, T. G., Ed.; Wiley: New York, 1987; Vol. 2, pp 1–58.
- Li, B.; Johnson, A. E.; Mukamel, S.; Myers, A. B. *J. Am. Chem. Soc.* **1994**, *116*, 11039.
- Frisch, M. J.; Trucks, G. W.; Schlegel, H. B.; Scuseria, G. E.; Robb, M. A.; Cheeseman, J. R.; Montgomery, J. A., Jr.; Vreven, T.; Kudin, K. N.; Burant, J. C.; Millam, J. M.; Iyengar, S. S.; Tomasi, J.; Barone, V.; Mennucci, B.; Cossi, M.; Scalmani, G.; Rega, N.; Petersson, G. A.;

- Nakatsuji, H.; Hada, M.; Ehara, M.; Toyota, K.; Fukuda, R.; Hasegawa, J.; Ishida, M.; Nakajima, T.; Honda, Y.; Kitao, O.; Nakai, H.; Klene, M.; Li, X.; Knox, J. E.; Hratchian, H. P.; Cross, J. B.; Bakken, V.; Adamo, C.; Jaramillo, J.; Gomperts, R.; Stratmann, R. E.; Yazyev, O.; Austin, A. J.; Cammi, R.; Pomelli, C.; Ochterski, J. W.; Ayala, P. Y.; Morokuma, K.; Voth, G. A.; Salvador, P.; Dannenberg, J. J.; Zakrzewski, V. G.; Dapprich, S.; Daniels, A. D.; Strain, M. C.; Farkas, O.; Malick, D. K.; Rabuck, A. D.; Raghavachari, K.; Foresman, J. B.; Ortiz, J. V.; Cui, Q.; Baboul, A. G.; Clifford, S.; Cioslowski, J.; Stefanov, B. B.; Liu, G.; Liashenko, A.; Piskorz, P.; Komaromi, I.; Martin, R. L.; Fox, D. J.; Keith, T.; Al-Laham, M. A.; Peng, C. Y.; Nanayakkara, A.; Challacombe, M.; Gill, P. M. W.; Johnson, B.; Chen, W.; Wong, M. W.; Gonzalez, C.; Pople, J. A. *Gaussian 03*, revision C.02; Gaussian, Inc.: Wallingford, CT, 2004.
- (43) Schaftenaar, G.; Noordik, J. H. *J. Comput.-Aided Mol. Des.* **2000**, *14*, 123.
- (44) Durig, J. R.; Pan, C. H.; Klaeboe, P.; Aleksa, V.; Guirgis, G. A. *Spectrochim. Acta, Part A: Molec. Biomolec. Spectrosc.* **2003**, *59*, 2151.
- (45) Guirgis, G. A.; Nashed, Y. E.; Durig, J. R. *J. Mol. Struct.* **1999**, *510*, 13.
- (46) Guirgis, G. A.; Nashed, Y. E.; Durig, J. R. *Spectrochim. Acta, Part A: Molec. Biomolec. Spectrosc.* **2000**, *56*, 1065.
- (47) Veroni, I.; Rontoyianni, A.; Mitsopoulou, C. A. *Dalton Trans.* **2003**, 255.
- (48) Wootton, J. L.; Zink, J. I. *J. Am. Chem. Soc.* **1997**, *119*, 1895.
- (49) Shin, K. S. K.; Zink, J. I. *J. Am. Chem. Soc.* **1990**, *112*, 7148.
- (50) Godbout, J. T.; Pietrzykowski, M. D.; Gould, I. R.; Goodman, J. L.; Kelley, A. M. *J. Phys. Chem. A* **1999**, *103*, 3876.
- (51) Phillips, D. L.; Myers, A. B. *J. Raman Spectrosc.* **1997**, *28*, 839.
- (52) Grafton, A. K.; Wheeler, R. A. *J. Comput. Chem.* **1998**, *19*, 1663.
- (53) Grafton, A. K.; Wheeler, R. A. *Comput. Phys. Commun.* **1998**, *113*, 78.
- (54) Waterland, M. R.; Stockwell, D.; Kelley, A. M. *J. Chem. Phys.* **2001**, *114*, 6249.
- (55) Waterland, M. R.; Kelley, A. M. *J. Phys. Chem. A* **2001**, *105*, 8385.
- (56) Petrenko, T.; Ray, K.; Wieghardt, K. E.; Neese, F. *J. Am. Chem. Soc.* **2006**, *128*, 4422.
- (57) Howell, S. L.; Gordon, K. C. *J. Phys. Chem. A* **2004**, *108*, 2536.
- (58) Schoonover, J. R.; Omberg, K. M.; Moss, J. A.; Bernhard, S.; Malueg, V. J.; Woodruff, W. H.; Meyer, T. J. *Inorg. Chem.* **1998**, *37*, 2585.
- (59) Gamelin, D. R.; George, M. W.; Glyn, P.; Grevels, F.-W.; Johnson, F. P. A.; Klotzbuecher, W.; Morrison, S. L.; Russell, G.; Schaffner, K.; Turner, J. J. *Inorg. Chem.* **1994**, *33*, 3246.
- (60) Dattelbaum, D. M.; Omberg, K. M.; Hay, P. J.; Gebhart, N. L.; Martin, R. L.; Schoonover, J. R.; Meyer, T. J. *J. Phys. Chem. A* **2004**, *108*, 3527.